

Semiconductor Manufacturing, pp. 217-218, Tokyo (June 1994).

20. Y. Shirai, M. Narazaki, and T. Ohmi, in *Proceedings of IEICE Trans. Electron.*, Vol. E79-C, No. 3, 385-389

(1996).

21. Y. Ikezoe, S. Matsuoka, M. Takebe, and A. Viggiano, *Gas Phase Ion-Molecule Reaction Rate Constants Through 1986*, Maruzen, Tokyo (1987).

A Two-Dimensional Model of Chemical Vapor Infiltration with Radio-Frequency Heating

II. Strategies to Achieve Complete Densification

Vikas Midha and Demetre J. Economou*

Plasma Processing Laboratory, Department of Chemical Engineering, University of Houston, Houston, Texas 77204-4792, USA

ABSTRACT

A two-dimensional finite-element model is used to compare isothermal and radio-frequency-assisted chemical vapor infiltration of long cylindrical carbon preforms. Densification with radio-frequency heating at a constant input power initially occurs radially around the central zone and then axially toward the ends of the preform. This densification pattern results in significant entrapment of porosity at the center of the preform and requires a relatively long time for completion. A novel scheme for improved radio-frequency heating of long cylindrical preforms is proposed which entails insulating the axial ends of the preform, induction heating at a relatively high operating frequency, and linear ramping of input power with time. Simulations show that, under these conditions, radial "inside-out" densification can be achieved uniformly along the entire length of the preform. This scheme results in complete densification of the preform and reduces the overall processing time fivefold when compared to the conventional isothermal process.

Introduction

Chemical vapor infiltration (CVI) has emerged as a leading technique for fabricating fiber-reinforced ceramic composite materials. The conventional CVI process consists of diffusion and chemical reaction of a precursor gas under essentially isobaric and isothermal conditions to deposit solid material within the pores of a fibrous preform. This process, however, is extremely slow and expensive, since low operating temperatures are necessary for uniform densification of the preform. At higher temperatures, the rate of chemical reaction exceeds the rate of mass transfer, leading to premature plugging of pores at the surface of the preform and entrapment of porosity inside the material.

A promising modification to isothermal CVI is to use volumetric heating of the preform. Volumetric heating combined with heat losses from the surface produces an "inverted" temperature gradient in the preform. This temperature profile favors a faster rate of chemical reaction in the interior of the preform as opposed to the surface, thereby minimizing the effect of increased mass-transfer resistance with densification of the preform. CVI with volumetric heating has the potential to achieve rapid and complete densification of preforms. This process has been demonstrated experimentally using microwave,¹ or radio-frequency (RF) induction heating.²⁻⁴

Existing theoretical studies of CVI with volumetric heating are mostly restricted to one-dimensional (1D) models.⁵⁻⁹ Moreover, the power distribution due to electromagnetic radiation is treated as constant in both time and space, or constant in time with a distribution corresponding to the initial electrical properties of the preform.^{8,9} Recently we reported the development of a 2D finite element model for CVI with RF heating, which self-consistently accounts for the variation in the power distribution as the preform densifies.¹⁰ A mechanism was identified by which more power is deposited in the densified regions of the preform that can potentially lead to thermal runaway. Simulations show that densification of a cylindrical carbon preform proceeds in an "inside-out" manner from the central zone, first in the radial direction and then axially toward the ends. The simulat-

ed temperature profiles showed semiquantitative agreement with experimental results reported in the literature.

This study further examines the potential of using RF-assisted CVI (RFCVI) for the densification of cylindrical carbon preforms by the thermal decomposition of methane. First, 2D simulations of isothermal isobaric CVI are presented, since this is the most widely accepted mode of CVI. By studying the influence of operating temperature and pressure, we form a base case for comparison with RFCVI. To be a feasible process, RFCVI must provide a significant improvement in performance compared to isothermal CVI. Next, the densification behavior with RFCVI is compared to that with isothermal CVI. We examine the influence of key operating parameters of RFCVI including total input power, pressure, and the effect of insulation for improving performance. Based on our understanding of the physics of RFCVI, we develop a novel scheme for tailoring RF heating to achieve rapid and complete densification of cylindrical preforms.

Mathematical Model

Figure 1 shows a schematic of the CVI apparatus modeled in this study. A cylindrical 3D carbon preform is placed coaxially at the center of the reactor. A helical RF induction coil is used to heat the preform to the desired operating temperatures. The entire assembly is enclosed in a metallic chamber to contain radiation. Details of the mathematical model formulation and the finite-element solution were presented earlier in Ref. 10. Therefore, only the salient features of the model are repeated here and modifications in the mathematical formulation are emphasized. For convenience, the mathematical model may be divided into two modules: the electromagnetic (EM) module and the CVI module. The governing equations of the two modules are summarized in Table I.

The EM module solves Maxwell's equations for the electromagnetic fields and the power distribution in the preform due to the induction coil. Since the electrical properties of the material evolve with porosity over time periods of several hours, the electromagnetic oscillations are assumed to be time-harmonic in nature. This enables the solution of the electric field in the frequency-domain as opposed to the time-domain. Azimuthal symmetry is im-

* Electrochemical Society Active Member.

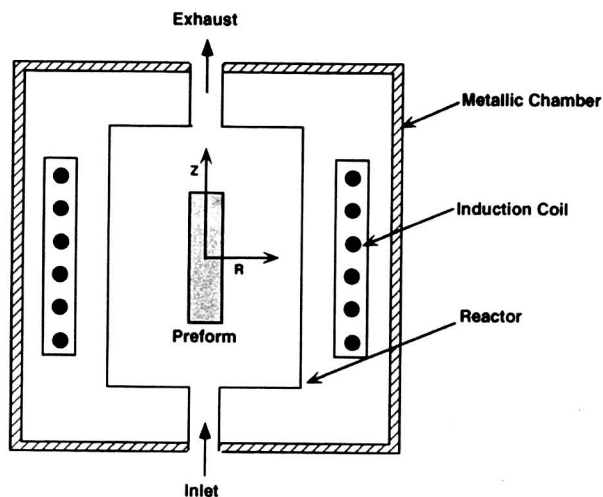


Fig. 1. Schematic of CVI reactor and RF induction coil studied.

posed by approximating the 3D geometry of the coils by a set of collinear loops of current around the reactor. The current is assumed to be constant along the length of the coil as capacitive coupling is negligible at the typical values of the operating frequency used in CVI applications.

Table I. Summary of governing equations.

1. Electromagnetic Module	
(1) Maxwell's Equations	$\nabla^2 E_0 + \frac{\omega^2}{c^2} K_C E_0 = -j\omega\mu_0 J_0^i$
(2) Ohm's Law	$W = \frac{1}{2} \sigma^e E ^2$
2. Chemical Vapor Infiltration Module	
(3a) Energy Balance	$\frac{\partial}{\partial t} ((1 - \epsilon^a) C_s C_p T - T_s) + \nabla \cdot N_H = W$
(3b)	$N_H = \sum_{i=1}^{N_c} N_i C_{p_i} (T - T_a) - k^e \nabla T$
(3c)	$N_S = n \left(h(T - T_a) + s \left(\frac{\pi}{2} \right)^2 e(T^4 - T_a^4) \right)$
(4) Mass Balance for <i>i</i> th Species	$\frac{\partial(\epsilon^a C_i)}{\partial t} + \nabla \cdot N_i = \sum_{r=1}^{N_r} v_{ir} R_r$
(5) Pressure Equation	$\frac{\partial}{\partial t} \left(\frac{\epsilon^a p}{RT} \right) + \nabla \cdot N_T = \sum_{i=1}^{N_c} \sum_{r=1}^{N_r} v_{ir} R_r$
(6) Solid Balance	$\frac{\partial \epsilon}{\partial t} = -\frac{M_s}{\rho_s} \sum_{r=1}^{N_r} v_{sr} R_r$
(7a) Dusty Gas Law	$N_i = J_i + x_i N_T$
(7b)	$\sum_{j \neq i}^{N_c} \frac{x_j J_i - x_i J_j}{\Delta_{ij}} = \frac{-p}{RT} \nabla x_i - \frac{x_i}{RT} \left(1 - \frac{1}{D_i^e} \sum_{s=1}^{N_c} \frac{x_s}{D_s^e} \right) \nabla p$
(7c)	$N_T = \frac{\sum_{s=1}^{N_c} \frac{J_s}{D_s^e}}{\sum_{s=1}^{N_c} \frac{x_s}{D_s^e}} - \frac{1}{RT} \left(\frac{Bp}{\mu} + \frac{1}{\sum_{s=1}^{N_c} \frac{x_s}{D_s^e}} \right) \nabla p$
(8) Reaction Kinetics $CH_4 \rightarrow C + 2H_2$	$R_{CH_4} = k_1 C_{CH_4} \exp[-E_1/(RT)]$

The value of this current is self-consistently adjusted during the densification process to maintain a specified value of total power input in the preform.

The CVI module consists of the governing equations for energy balance, gas-phase mass balances, and solid balance for the evolution of porosity in the preform. The energy balance accounts for heat conduction and convection in the preform with a time-averaged power input from the RF induction coil. Heat loss occurs from the surfaces of the preform due to convection and radiation. As described in Ref. 4, the effective external surface area available for radiation is increased by a factor of $(\pi/2)^2$ over the geometric area to reflect the curved surfaces of the fiber bundles. Mass transfer of the gas mixture is modeled using the Dusty gas model for the molar flux of each chemical species. The Dusty gas model¹¹ accounts for multicomponent diffusion, Knudsen diffusion, and viscous flow of the gas in the preform. The decomposition of methane is modeled by first-order kinetics based on the methane concentration. The evolution of preform porosity is calculated from an overall solid-phase mass balance as carbon is deposited in the pores of the preform.

In our previous work,¹⁰ the power input due to induction heating (W) was weighted with the solid fraction $(1 - \epsilon)$ in the energy balance to emphasize that only the solid fraction of the preform is directly heated by the electromagnetic waves. The effective electrical conductivity of the composite used in Ohm's law (Eq. 2, Table I) for power deposition in the preform was estimated by the linear relation

$$\sigma^e = \sigma_s (1 - \epsilon) \quad [1]$$

In that previous work,¹⁰ the volume integral of the weighted power input in the preform, $W(1 - \epsilon)$, was kept constant throughout the densification process to simulate constant input power conditions. If Poynting's theorem¹² is considered, the total power input due to the electromagnetic waves must be conserved. Since the electromagnetic fields are confined by a metallic chamber containing the CVI reactor, all power from the electromagnetic fields must be deposited in the preform (i.e., all the electric power is deposited in the form of thermal power in the preform). This assumes that power dissipation in the metallic chamber is negligible, which should be true if the metallic chamber walls are far enough from the coils. Therefore, in this study the heat source term in the energy balance is not weighted by the solid fraction (Eq. 3a in Table I). The two approaches are equivalent, since the right hand side of Eq. 3a is kept constant in both cases. Moreover, a more suitable expression for calculating the effective electrical conductivity of the preform is considered for calculating the power deposition profile in the preform.

In addition to the calculation of effective electrical conductivity, modeling the densification process requires the calculation of the effective thermal conductivity of the preform and the effective binary and Knudsen diffusivities of the gaseous species. Effective medium theory (EMT) has been applied in the literature for the calculation of thermal conductivity^{9,13} and effective diffusivities of gaseous species in the preform.¹⁴ The EMT, however, may give less accurate results for 3D pore morphologies compared to 2D morphologies, especially near the percolation limit.¹⁵ For instance, applying EMT for the calculation of the effective electrical conductivity of a 3D carbon preform gives the relation

$$\epsilon \frac{(\sigma_s - \sigma^e)}{\sigma_s + \left(\frac{Z}{2} - 1 \right) \sigma^e} + (1 - \epsilon) \frac{(\sigma_g - \sigma^e)}{\sigma_g + \left(\frac{Z}{2} - 1 \right) \sigma^e} = 0 \quad [2]$$

where Z is the coordination number. Neglecting the gas-phase electrical conductivity in comparison to the solid-phase electrical conductivity and substituting a coordination number of 6^{9,13} simplifies Eq. 2 to

$$\sigma^e = \sigma_s \left(1 - \frac{3}{2} \epsilon \right) \quad [3]$$

From this expression, a 3D preform with a porosity of 0.667 would have zero effective electrical conductivity. The same result is also true for the effective thermal conductivity of the preform. This conclusion clearly disagrees with experimental results which show rapid RF induction heating of 3D carbon preforms, with initial porosity of 0.7, to temperatures ranging from 1400 to 1600 K.⁴

For a binary mixture of a conductor in a purely insulating phase, percolation theory¹⁶ predicts that the effective electrical conductivity near the percolation threshold is given by the relation

$$\sigma^e \propto \left(\frac{1 - \epsilon}{\epsilon_p} \right)^n \quad [4]$$

where ϵ_p is the percolation threshold and n is a pore-structure dependent parameter, usually greater than 1. For ellipsoidal grain structures, the value of ϵ_p is usually close to 0.84 and the values of n generally lie in the range 1.65–2.0. However, higher values of ϵ_p and n are expected when the conducting particles have extreme geometries like the fiber structures considered here. Carmona et al.¹⁷ measured the effective electrical conductivity of carbon and graphite fibers in epoxy for different aspect ratios and observed percolation threshold values close to 0.99 and n values of 1.95 for carbon fibers and 3.1 for graphite fibers. Similarly, Tomadakis and Sotirchos¹⁸ conducted Monte Carlo simulations for fiber structures and found a percolation value of 0.963.

The general effective medium theory (GEMT)¹⁹ is a phenomenological model with a mathematical form similar to the percolation equation. For a conducting material present in a purely insulating phase, the effective electrical conductivity is given by

$$\sigma^e = \sigma_s \left(1 - \frac{\epsilon}{\epsilon_p} \right)^n \quad [5]$$

Figure 2 compares the effective value of electrical conductivity from the GEMT model for $\epsilon_p = 0.963$ and $n = 2$ to the EMT of Eq. 3 and a fit to Monte Carlo simulations for fiber structures reported in the literature.^{9,13} The GEMT model shows fair agreement with the Monte Carlo simulations for all values for porosity. Both the GEMT model and the Monte Carlo results agree with the EMT for porosity values less than 0.5. The GEMT model was used in the present simulations to calculate the effective electrical and thermal conductivity of the preform during the densification process.

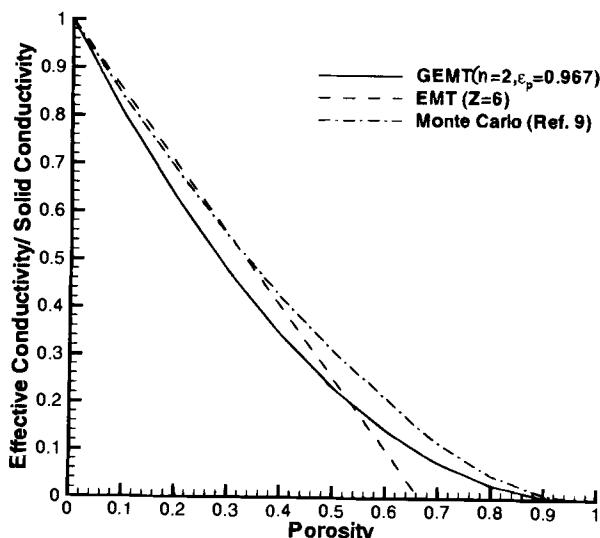


Fig. 2. Effective electrical and thermal conductivity as predicted by different pore models. GEMT refers to Eq. 5, EMT refers to Eq. 3. Monte Carlo results from Ref. 9 are also shown.

In contrast to electrical and thermal transport which occur primarily in the solid, mass transport of the gas species occurs in the void fraction of the preform. Our previous results on RFCVI¹⁰ were based on a randomly overlapping capillary model of uniform-sized pores. The pore-structure dependent mass-transfer parameters were then defined by

$$S = \frac{-2(1 - \epsilon) \ln(1 - \epsilon)}{\tau_p}, \quad S_1 = \frac{D_{i1}^e}{D_{i1}} = \frac{\epsilon^a}{\eta},$$

$$S_2 = \frac{D_{i2}^e}{D_{i2}} = \frac{\epsilon^a}{\eta} \left(\frac{r_p}{r_p^*} \right), \quad B = \frac{\epsilon^a}{\eta} \frac{r_p^2}{8} \quad [6]$$

where S is the internal surface area per unit volume (solid plus void) of the preform, τ_p is the radius of the capillary pores, r_p^* is a reference value of pore radius for the calculation of Knudsen diffusivity, and η is the tortuosity factor. The percolation threshold for the capillary model is zero and the accessible porosity is always equal to the total porosity of the preform. The tortuosity factor was assumed to be constant at a value of three for all values of porosity.^{20,21} Monte Carlo simulations, however, show that the tortuosity value can deviate significantly from this value, especially for low preform porosity.¹⁸

In this paper we use a randomly overlapping uniform radius fiber model²¹ (as opposed to a pore model used in Ref. 10) and combine the former model with the GEMT equation for calculating effective diffusivities. The effective values of the mass-transfer parameters are then found as

$$S = \frac{-2\epsilon \ln \epsilon}{r_f}, \quad S_1 = \left(\frac{\epsilon - \epsilon_p}{1 - \epsilon_p} \right)^n, \quad S_2 = \left(\frac{\epsilon - \epsilon_p}{1 - \epsilon_p} \right)^n \left(\frac{r_p}{r_p^*} \right)^n,$$

$$B = \left(\frac{\epsilon - \epsilon_p}{1 - \epsilon_p} \right)^n \frac{r_p^2}{8} \quad [7]$$

where r_f is the fiber radius and τ_p is the pore radius defined by the relation

$$\tau_p = \frac{2\epsilon}{S} \quad [8]$$

A value of $n = 2$ and a percolation threshold of 0.037 are adopted which are consistent with the values used for calculating the effective electrical and thermal conductivity. Figure 3 compares the effective binary and Knudsen diffusivities for the fiber and capillary pore models. In both cases the initial pore radius is equal to the reference pore radius

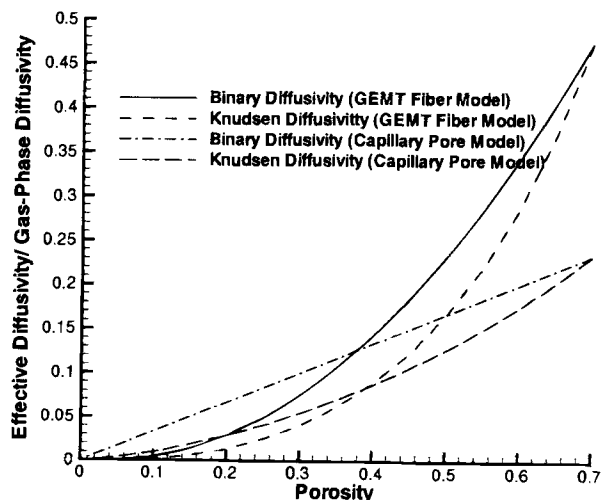


Fig. 3. Effective binary and Knudsen diffusivity predicted by different pore models. GEMT Fiber Model refers to a randomly overlapping fiber model representation of the preform (Eq. 7), and the randomly overlapping capillary pore model has a constant tortuosity factor of 3 (Eq. 6).

Table II. Parameter values used in the simulation (unless noted otherwise in text).

Preform radius	0.0142 m
Preform height	0.0762 m
Preform initial porosity	0.70
Heat-transfer coefficient	10 W/(m ² K)
Carbon thermal conductivity	150 W/(mK)
Carbon specific heat	0.675 kJ/(kg K)
Carbon density	2270 kg/m ³
Carbon emissivity	0.86
Frequency	50 kHz
Carbon electrical conductivity	5 × 10 ⁴ S/m
Total initial power	6 kW
Nominal pressure	100 Torr
Initial fiber radius	10 μm
Ambient temperature	300 K
Ambient CH ₄ mole fraction	0.6
Ambient Ar mole fraction	0.4

used for the calculation of effective Knudsen diffusivity. The effective diffusivities with the fiber model are considerably higher for high values of porosity but also decay at a faster rate than the diffusivities from the capillary pore model. Therefore, we initially expect a higher rate of mass transfer with the fiber model which diminishes more rapidly as the preform densifies. The fiber model is adopted for all the simulations presented in this work, and differences in the densification behavior due to pore-structure representation are discussed.

An important limitation of the transport property models presented here is that the effect of fiber orientation is not included. The assumption of randomly overlapping fibers or randomly overlapping capillary pores gives effective transport property values which are isotropic whereas, depending on the weave architecture of the preform, actual values may exhibit a significant amount of anisotropy. Although such anisotropy can easily be incorporated in the governing equations by employing a tensor representation of the effective values instead of a scalar representation, only isotropic values are used in the simulations presented herein.

Numerical Method of Solution

The governing equations were discretized spatially using a Galerkin finite-element formulation²² with linear quadrilateral elements. From symmetry considerations, only the upper right quadrant of the metallic chamber in the *r-z* plane was considered. Up to 800 elements were used to discretize the preform region for the CVI module with an additional 400 elements used to discretize the remainder of the metallic chamber for the EM module. The EM module resulted in a set of complex arithmetic algebraic equations which were solved directly using a complex matrix solver. The CVI module resulted in a set of

ordinary differential equations (ODE) which were integrated using LSODI,²³ a variable-order, variable time-step ODE solver. Each function evaluation of the ODE solver included a call to the EM module to determine the power distribution in the preform self-consistently. The central processing unit (CPU) time for each run was of the order of 1 h on an HP 125 MHz workstation.

Results and Discussion

The parameter values used in simulating the infiltration of a cylindrical carbon preform by the thermal decomposition of methane are shown in Table II.^{24,25} Any departure from these values is reported separately in the discussion of the results. In order to characterize the performance of a CVI operation, we consider the following "figures of merit":

1. Total processing time (t_p), which directly relates to the economics of the process.

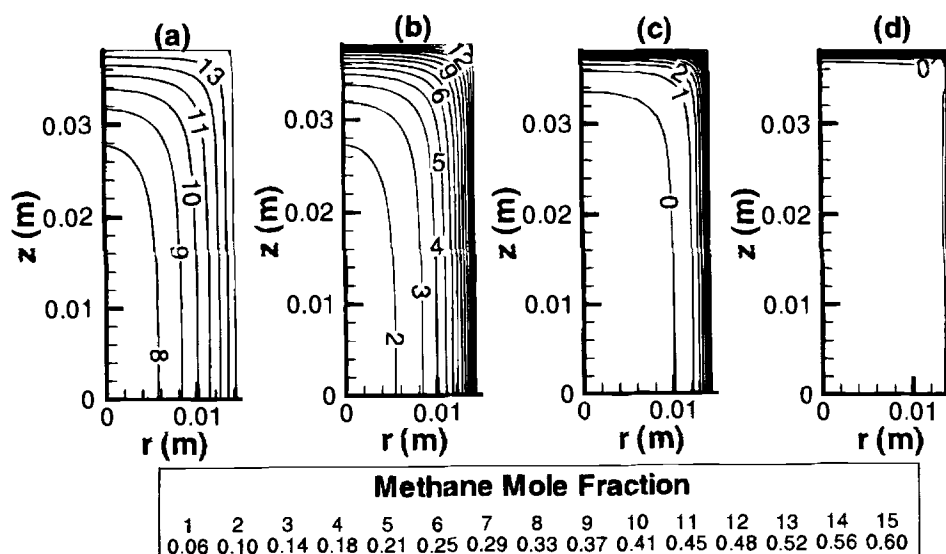
2. Final spatially averaged porosity (ϵ_f), which determines the final bulk density and the mechanical properties of the final composite material.

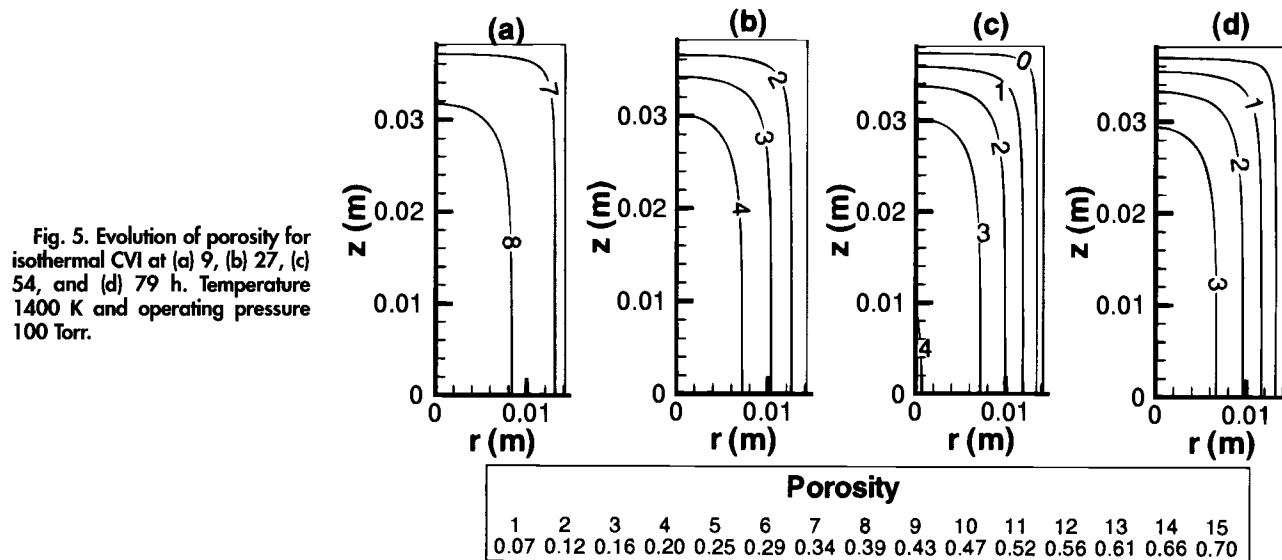
3. Maximum value of entrapped porosity (ϵ_{max}), within the preform. We expect that the final mechanical properties of the preform will also be affected by how the entrapped porosity is distributed in the volume of the preform. For instance, the properties of a preform with all the entrapped porosity localized in a small region at the center will not be the same as those of a preform with the entrapped porosity distributed uniformly throughout its volume.

Another important factor which is critical in determining the final mechanical properties of the composite is the morphology of the carbon deposited by the infiltration process. This morphology may vary not only at different operating conditions but also within different parts of the finished product if, for example, large temperature gradients are present during RFCVI. Unfortunately, a priori prediction of the type of deposit morphology is not possible with the present model.

Isothermal CVI.—First, isothermal isobaric CVI of the carbon preform is considered. In this case, the RF induction coil may be used to heat a susceptor lining the walls of the reactor. The susceptor in turn heats the preform to the desired operating temperature by radiation. Figures 4 and 5 show the evolution of methane mole fraction and preform porosity during isothermal CVI at a temperature of 1400 K and a pressure of 100 Torr. Isothermal CVI for the elongated preform geometry is essentially a 1D process with densification occurring along the entire perimeter of the preform. Densification proceeds in an "outside-in" pattern with a faster rate of densification at the edges than at the center of the preform. This densification pattern is due to mass-transfer

Fig. 4. Evolution of methane mole fraction for isothermal CVI at (a) 9, (b) 27, (c) 54, and (d) 79 h. Temperature 1400 K and operating pressure 100 Torr.





limitations of methane within the preform. As the exterior of the preform densifies, diffusional resistance for the precursor gases increases, leading to the entrapment of porosity in the center of the preform. The entrapped porosity is almost uniformly distributed throughout the core of the preform. The maximum value of entrapped porosity is located at the center of the preform.

For a given preform, the operating parameters available for improving the performance of isothermal CVI are temperature and pressure. Figure 6 shows the effect of operating temperature on the performance of isothermal CVI for a constant pressure of 100 Torr. Increasing the operating temperature reduces the processing time dramatically but only at the expense of more entrapped porosity at the center of the preform. The maximum value of porosity increases at a faster rate than the spatially averaged (bulk) porosity, which indicates that the mechanical properties of the composite material may deteriorate faster than what is reflected by the bulk density alone.

Figure 7 shows the effect of operating pressure on the performance of isothermal CVI at temperatures of 1300 and 1400 K. The processing time may be reduced significantly by increasing the operating pressure due to the presence of higher concentrations of precursor gas. However, since the binary diffusivities are inversely proportional to pressure, mass-transfer limitations become pronounced at higher pressures and lead to higher levels of entrapped porosity. As the operating pressure is reduced, Knudsen

diffusion begins to dominate earlier in the process over binary diffusion and eventually mass transport of the precursor gas in the preform becomes independent of pressure.

Figure 7 shows that both the spatially averaged (bulk) porosity and the maximum entrapped porosity increase monotonically with pressure for isothermal operation of 1400 K. At a temperature of 1300 K, the bulk porosity and maximum entrapped porosity increase as the pressure is increased from 200 to 300 Torr but remain fairly constant thereafter. Therefore, the effect of pressure is more pronounced at higher temperatures compared to lower ones. This is because densification occurs faster at the surface of the preform at higher temperatures and mass transfer effects become more important. At lower temperatures, densification occurs more uniformly along the radius of the preform and mass-transfer effects become less critical. At a temperature of 1300 K, although the final bulk porosity is relatively insensitive to pressure, the processing time increases significantly as pressure is lowered. Therefore, reduction in entrapped porosity in the preform requires a significant increase in processing time at low operating temperatures.

Determining the exact values of the optimal temperature and pressure for the given preform geometry would require an optimization procedure similar to that reported by Ofori and Sotirchos²⁶ with their 1D CVI model. This optimum, however, is restricted to the particular reaction kinetics considered in the model and the values of other parameters such as binary diffusivities of the gases in the

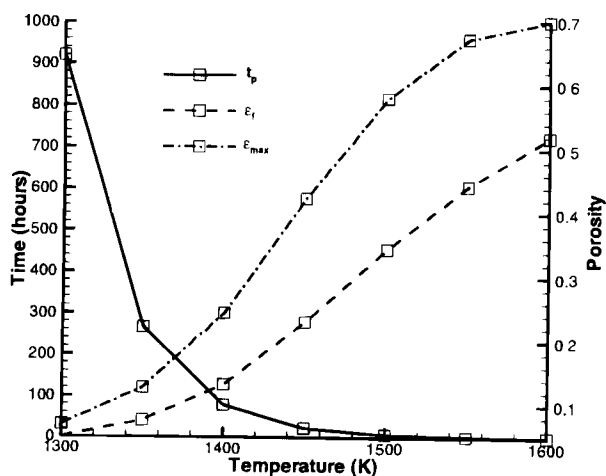


Fig. 6. Effect of operating temperature on the performance of isothermal CVI at 100 Torr pressure.

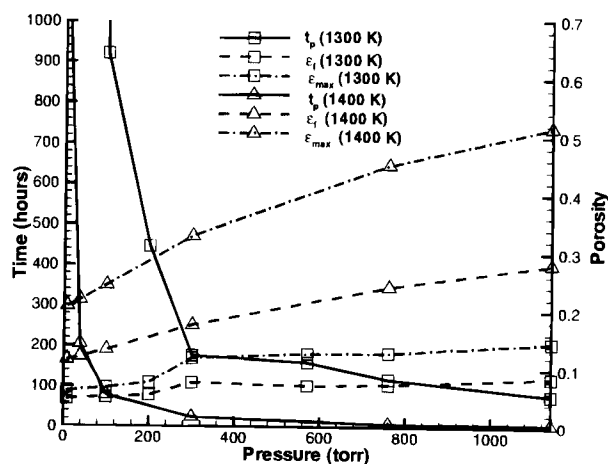


Fig. 7. Effect of operating pressure on the performance of isothermal CVI at 1300 K and 1400 K.

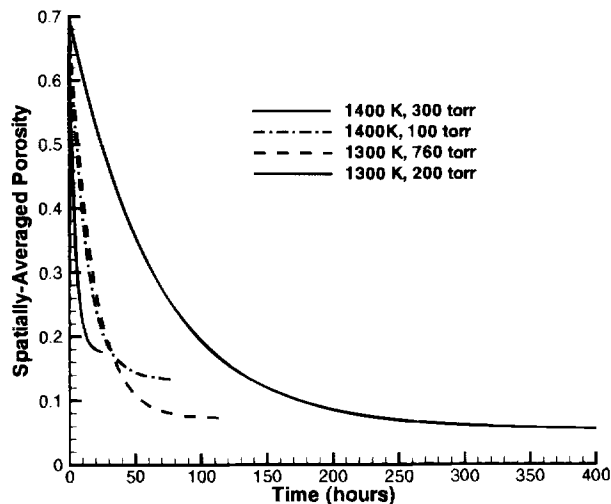


Fig. 8. Rate of densification (expressed as spatially averaged porosity vs. time) for isothermal CVI at 100 Torr and 1300 or 1400 K.

reaction mixture and pore-size of the preform. Since the focus of this study is a more general comparison of the densification behavior of isothermal CVI and RFCVI, we adopt a more straightforward approach to defining the base case conditions for comparison.

Figure 8 shows the evolution of the spatially averaged (bulk) porosity of the preform for operation at 1300 and 1400 K at different pressures. Pore plugging, signified by the curves in Fig. 8 turning horizontal, occurs earlier at higher temperatures. For designating any CVI operation as successful, we impose the condition that the final bulk porosity should be less than 10% of the initial porosity. For an initial porosity of 0.7, this condition would require a final bulk porosity less than 0.07. As shown earlier in Fig. 7, an operating temperature of 1400 K does not meet this requirement for any value of operating pressure. Furthermore, operation at 1300 K and 1 atm pressure yields rates of densification comparable to operation at 1400 K and 100 Torr pressure for all times and eventually produces considerably less entrapped porosity. Therefore operation at a temperature of 1300 K is considered superior to operation at 1400 K. In order to obtain a final porosity within 10% of the initial porosity at 1300 K, however, requires a reduction in the operating pressure to 200 Torr. Therefore, an operating temperature of 1300 K and pressure of 200 Torr are considered "optimal" with a processing time of about 300 h. For RFCVI to be superior compared to the isothermal process, densification of the

preform to comparable levels of bulk porosity should be possible in a processing time significantly less than 300 h.

Another important feature of isothermal CVI shown in Fig. 8 is that the rate of densification declines rapidly as the preform densifies. Therefore, the time required to densify the preform to the minimum attainable porosity is considerably longer than the time required to reach an intermediate level of porosity. For instance, the minimum attainable porosity for isothermal densification at 1300 K and 200 Torr is 0.06 and requires about 400 h of operation. However, the time required to reduce the bulk porosity from 0.7 to 0.12 is only 150 h, whereas reduction from a porosity of 0.12–0.06 requires an additional 250 h. The criterion used for estimating the processing time in this study requires that the final porosity be within 1% of the minimum attainable porosity for a given set of operating conditions. This provides conservative estimates of the processing time. The actual processing time may be reduced considerably depending on the economics and the desired mechanical properties of the final composite material.

RFCVI.—In RFCVI, the induction coil is used to directly heat the carbon preform to the desired operating temperature while the walls of the reactor are kept cool. With power deposited within the volume of the preform and cooling at the surfaces by convection and radiation, an "inverted" temperature profile is attained with the maximum temperature at the center of the preform. The precursor gas diffuses into the preform and reacts to deposit carbon within the pores. The lower concentration of the precursor deeper into the preform is more than compensated by the higher temperature there.

Figures 9–12 show the evolution of power density, temperature, methane mole fraction, and porosity in the upper-right quadrant of the preform during the densification process. Clearly, the densification behavior in RFCVI is more complicated compared to isothermal CVI. This is due to the strong coupling between EM, heat, and mass transport as a function of the evolving properties of the material.

Densification is initiated near the center of the preform but is quickly confined to the radial edges. As the effective electrical conductivity of the densified preform evolves, more power is deposited in the densified regions. This localized heating constitutes a thermal runaway mechanism and results in a rapid increase in temperature around the central axial plane of the preform. Since the total input power is kept constant by adjusting the induction coil current, more power deposition in the central zone implies that less power is absorbed by the axial ends of the preform, causing a drop in the temperature there. An off-axis peak in the radial temperature profile (Fig. 10b and c) signifies an increase in axial heat conduction toward the cooler ends of the preform

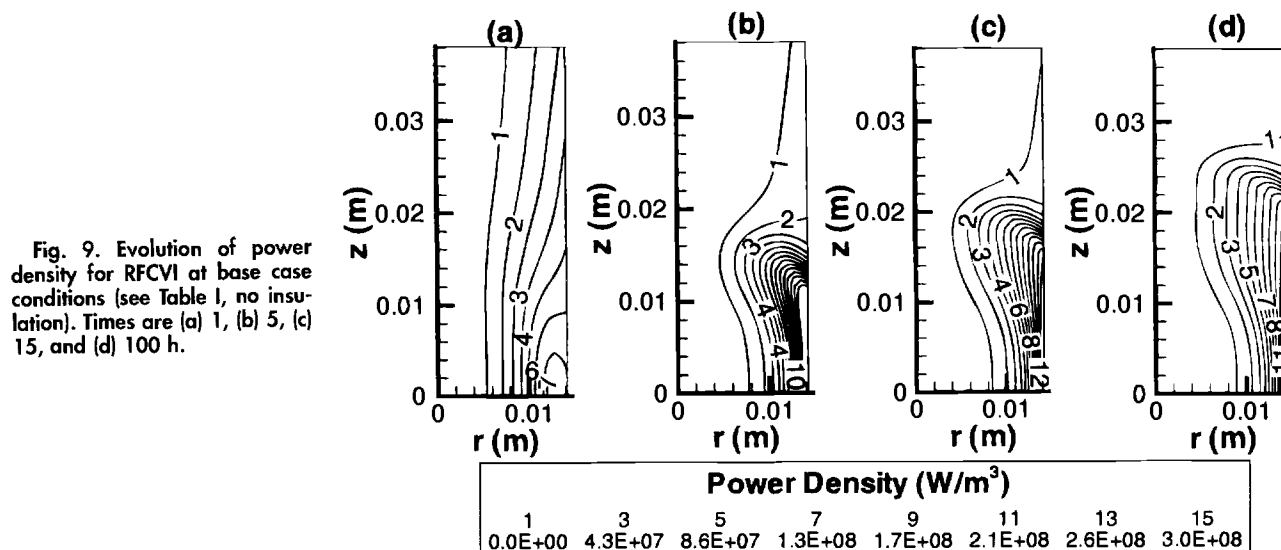


Fig. 9. Evolution of power density for RFCVI at base case conditions (see Table I, no insulation). Times are (a) 1, (b) 5, (c) 15, and (d) 100 h.

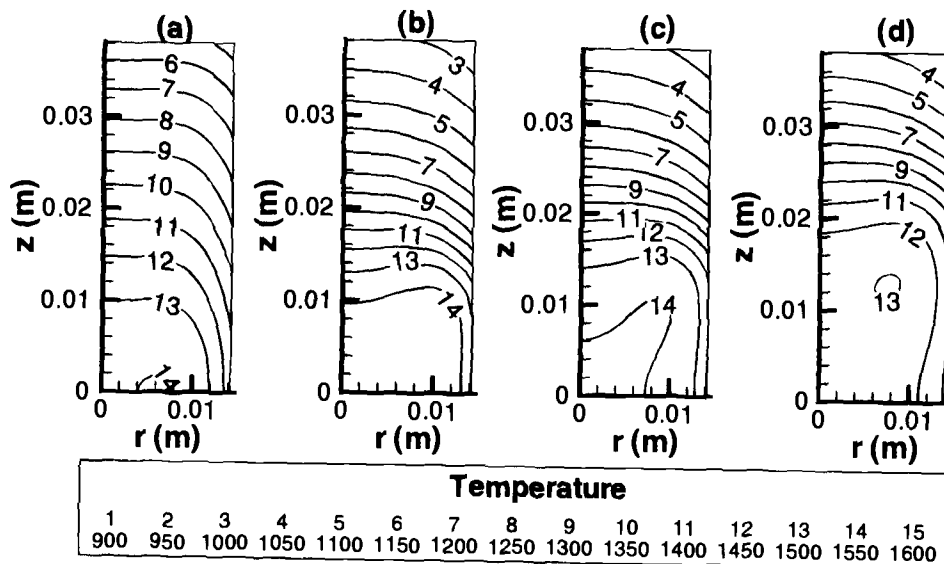


Fig. 10. Evolution of temperature for RFCVI at base case conditions (see Table I, no insulation). Times are (a) 1, (b) 5, (c) 15, and (d) 100 h.

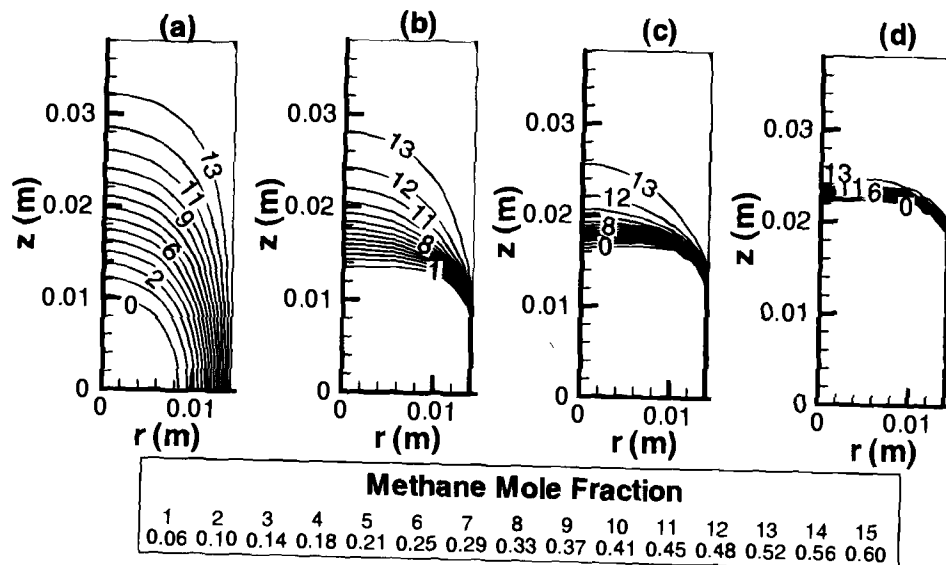


Fig. 11. Evolution of methane mole fraction for RFCVI at base case conditions (see Table I, no insulation). Times are (a) 1, (b) 5, (c) 15, and (d) 100 h at base conditions.

compared to radial heat conduction to the hot edges. The formation of this off-axis temperature peak has been observed in experiments with a similar system reported in the literature.⁴

At the elevated temperatures, mass-transfer limitations become significant and cause the formation of a sharp concentration front of the reactant around the center of the preform (Fig. 11). Depletion of reactant leads to the forma-

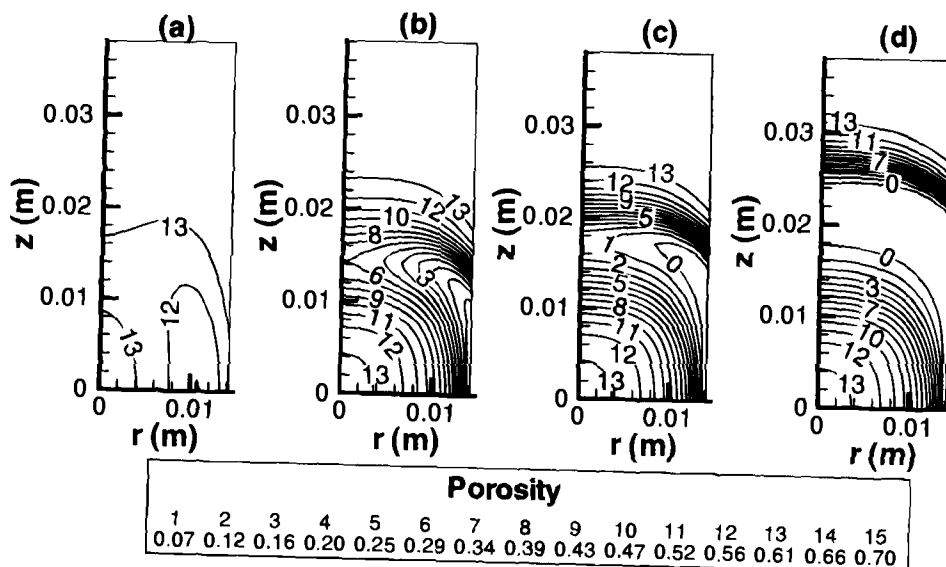


Fig. 12. Evolution of porosity for RFCVI at base case conditions (see Table I, no insulation). Times are (a) 1, (b) 5, (c) 15, and (d) 100 h.

tion of entrapped porosity around the center. Subsequent densification occurs axially as the reactant concentration front retreats toward the axial ends of the preform. Since the region of localized heating also expands with densification of the preform, the off-axis temperature peak splits into two peaks which migrate toward the axial ends of the preform (Fig. 10d). No additional entrapped porosity is formed during the axial densification of the preform.

The results shown in Fig. 9–12 correspond to the fiber model for transport properties. These results are qualitatively similar to those reported earlier in Ref. 10 with the capillary pore model for pore structure. A closer comparison of the results shows that only the numerical values (such as the level of entrapped porosity at the center) are different in Fig. 12 compared to Fig. 8 of Ref. 10. This is due to the combination of higher input power (6 kW compared to 4 kW) and the different transport property values. In addition, varying the exponent n over the range 1.65–3 in the GEMT equation for the calculation of effective properties produced no distinct change in the overall densification pattern. Our earlier study¹⁰ discusses in detail how this densification behavior agrees with experimental results reported in the literature.

Comparison of RFCVI with isothermal CVI.—In contrast to isothermal CVI, densification of the preform with RFCVI is a complicated 2D process. Densification proceeds in an “inside-out” pattern initially in the radial direction around the central zone of the preform and subsequently in the axial direction toward the ends of the preform. This behavior indicates that the preform geometry plays a more important role in RFCVI compared to isothermal CVI. Although low bulk porosity values are achieved with RFCVI in our study, the maximum porosity is considerably higher in RFCVI compared to isothermal CVI. This is because all the entrapped porosity is confined to a small region at the center of the preform in RFCVI, whereas it is distributed over a much larger volume of the preform in isothermal CVI. In fact, the maximum porosity is close to the initial porosity in RFCVI, indicating that only minimal densification occurs at the center of the preform. We suspect that the mechanical properties of a composite material with negligible densification at the center are quite poor in comparison to preforms with similar bulk densities but with distributed porosity.

Figure 13 compares the rate of densification of the preform with RFCVI to the isothermal case. Initially, rapid densification of the preform is possible with the RFCVI mainly due to thermal runaway at the center of the preform. This trend also agrees with experimental results which show a significant increase in bulk density within the first

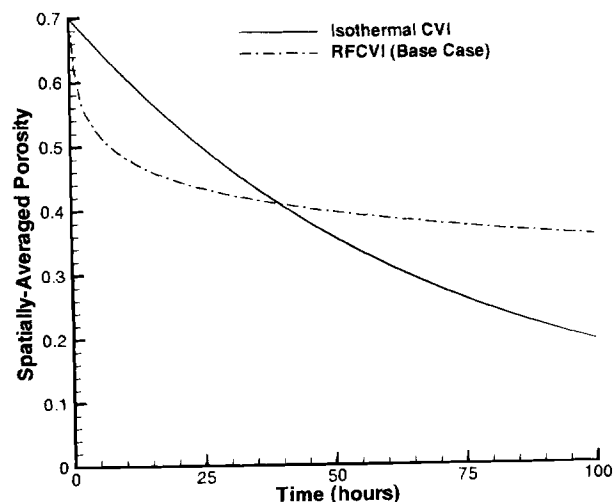


Fig. 13. Comparison of rate of densification with isothermal CVI (1300 K, 100 Torr) and RFCVI at base case conditions (see Table I, no insulation).

30 h of processing. However, the initial period of rapid densification of the preform with RFCVI also corresponds to the time at which all the entrapped porosity is formed. As the preform begins to densify axially, no additional entrapped porosity is formed, but the rate of densification is inhibited by the low temperatures at the ends of the preform. Since the densification pattern is always “radial” along the entire perimeter of the preform in isothermal CVI, the rate of densification with isothermal CVI eventually overtakes the rate of densification with RFCVI. Therefore, a considerably longer time is required with RFCVI compared to isothermal CVI for complete densification of the preform.

It is clear from this study that a radial densification pattern is superior to an axial densification pattern for the long cylindrical preform geometry. Therefore, the influence of operating parameters for RFCVI was examined for improving the densification behavior. Although the numerical values of entrapped porosity and processing time change, the overall densification pattern shown in Fig. 12 is surprisingly similar with respect to the parameter values. For higher values of input power, the center of the preform heats up to higher temperatures and the radial densification becomes confined only to the edges of the preform. Subsequent densification then proceeds axially toward the ends of the preform similar to that shown in Fig. 12. Although the processing time may be reduced by increasing the input power level, the entrapped porosity at the center of the preform increases and the maximum porosity rapidly approaches the initial porosity of the preform.

The effect of pressure on the densification behavior is similar to that of input power. As pressure is increased the concentration of the reactant gas increases leading to faster rates of reaction. However, increased mass-transfer resistance at higher pressures increases the value of entrapped porosity and the maximum porosity.

The densification behavior also proved to be relatively insensitive to the configuration of the induction coil. The effect of coil configuration was studied by altering the current in the individual loops of the coil. Even when all the current was confined to the outermost loops of the coil, the temperature of the axial ends of the preform was lower than the center and eventually densification proceeded outwardly from the center to the axial ends of the preform. This is because after the initial transient heating of the preform, the pseudo-steady axial temperature profiles due to induction heating always peaked at the center of the preform. Once densification is initiated at the center of the preform, the power distribution changed to deposit more power in the densified regions that led to the same behavior as shown in Fig. 12.

Tailoring RF heating for long cylindrical preforms.—Based on our understanding of the RFCVI process, we propose the following modifications for improved infiltration of long cylindrical preforms.

Insulate the ends of the preform.—One of the major reasons for the slow rate of densification with RFCVI (Fig. 13) is the low temperature at the ends of the preform. As densification is initiated, more power is deposited at the center compared to the axial ends. For a constant input power, the temperature of the axial ends of the preform remains low even as the center is heated. The ends slowly heat up only as the preform densifies in the axial direction. This problem is directly related to the elongated geometry of the preform and would become more severe as the aspect ratio is increased.

In order to reduce the axial temperature gradient in long preforms, we propose insulating the ends with a dielectric material. This way, all heat loss is now limited to the radial edges of the preform. This favors a more uniform axial temperature distribution with a higher temperature at the axial ends of the preform compared to the case without insulation. A radial temperature profile promotes simultaneous densification along the entire length of the preform as opposed to an axial densification pattern.

Use higher RF frequency.—The origin for the entrapped porosity in RFCVI is the thermal runaway mechanism by which more power is deposited in regions of the preform which are already densified. We propose that increasing the operating frequency will reduce and to some extent reverse the coupling between power density and preform porosity.

The penetration depth of the electromagnetic fields into the preform is given by Ref. 12

$$\delta_p = \sqrt{\frac{1}{\pi\mu_0\sigma^e f}} \quad [9]$$

where f is the frequency of the electromagnetic oscillations. The operating frequency of 50 kHz used in the simulations so far corresponds to the value used in experiments reported in the literature. This frequency is chosen so that the penetration depth would be equal to the radius of the fully densified preform. However, if the operating frequency is selected so that the penetration depth is equal to the radius at the initial porosity, the penetration depth of the electromagnetic fields in the densified regions of the preform decreases as the effective electrical conductivity increases. The electromagnetic fields penetrate more into the porous parts of the preform compared to the densified parts. Therefore, as the induction-coil current is adjusted to maintain a specified power in the preform, an increase in the coil current effectively results in more power being deposited in the porous parts of the preform. If the center of the preform densifies first, more power is deposited at the ends of the preform and localized heating is minimized.

Note that there is a limited range of frequencies which are acceptable for RF induction heating of the preform. If the operating frequency is too low then the coupling between power deposition and solid is strong and can lead to localized heating. If the operating frequency is too high, then a large coil current is required to deposit the desired power into the preform. This effect can be minimized to some extent by moving the coils closer to preform. Eventually, however, maintaining a specified value of input power in the preform will be impossible. We chose an operating frequency of 500 kHz for which the penetration depth is 1 cm at the initial porosity of 0.7 and 0.3 cm at the percolation threshold of 0.037 when the preform becomes inaccessible to further infiltration by the reactant gas.

Use power ramping.—Another important operating parameter available in RFCVI is the power input from the RF induction coil as a function of time. The results shown in Fig. 12 are based on a constant total input power where the current in the coil is continuously adjusted to maintain that power. Since densification occurs slowly over a time scale of several dozen hours, the input power may be

adjusted with time through a matching network to improve performance.

Morell et al.^{6,7} have proposed schemes for reducing the processing time, including a step increase in power level and pulsed power. For the conditions of the present study, however, 2D simulations show that a step increase in the input power as the preform densifies axially results in the additional entrapment of porosity in the preform. More power is deposited at the center of the preform, causing the center temperature to rise and the reactant concentration front to rapidly retreat to the ends. Continuous pulsing of power between two power levels yielded results intermediate to using constant power at the two levels separately. Therefore, it should be possible to duplicate the densification with pulsed power by using a constant intermediate power level. In this study, we propose a simple linear ramping of power as the preform densifies. Initially at low power levels, the preform temperature is low and densification occurs in the interior of the preform. As the preform densifies a gradual increase in power enables a faster rate of carbon deposition without additional entrapment of porosity.

Figures 14–17 show the evolution of power, temperature, methane mole fraction and porosity as a function of time for the modified heating scheme. The ends of the preform are insulated, the RF frequency is 500 kHz as opposed to 50 kHz, and the input power level is linearly ramped starting from 4000 W at a rate of 20 W/h. A relatively high pressure of 1 atm is also used in the simulations to improve the overall rate of densification.

Initial densification occurs at the center of the preform similar to the previous case (Fig. 17) leading to some localized heating at the center compared to the ends of the preform. However, as the radial edges of the preform begin to densify, the penetration depth of the electric fields begin to diminish at the relatively high operating frequency. RF heating with a low penetration depth at the center favors more power deposition at the upper corners of the preform which are exposed radially and axially to the electromagnetic fields. The axial peak in power density at the center of the preform gradually decays and new peaks are formed at the ends of the preform (Fig. 14b and c). This indicates that localized heating of the center of the preform is avoided with the modified set of conditions. As the preform densifies further, power is deposited uniformly along the entire length of the preform (Fig. 14d). The peak value of the power density also rises steadily as the total power into the preform is ramped as a function of time.

The effect of evolving power-density profiles is directly reflected in the evolution of the preform temperature (Fig. 15). The initial peak in temperature is located at the center of the preform where densification is initiated. Note that the axial variation of temperature is much smaller

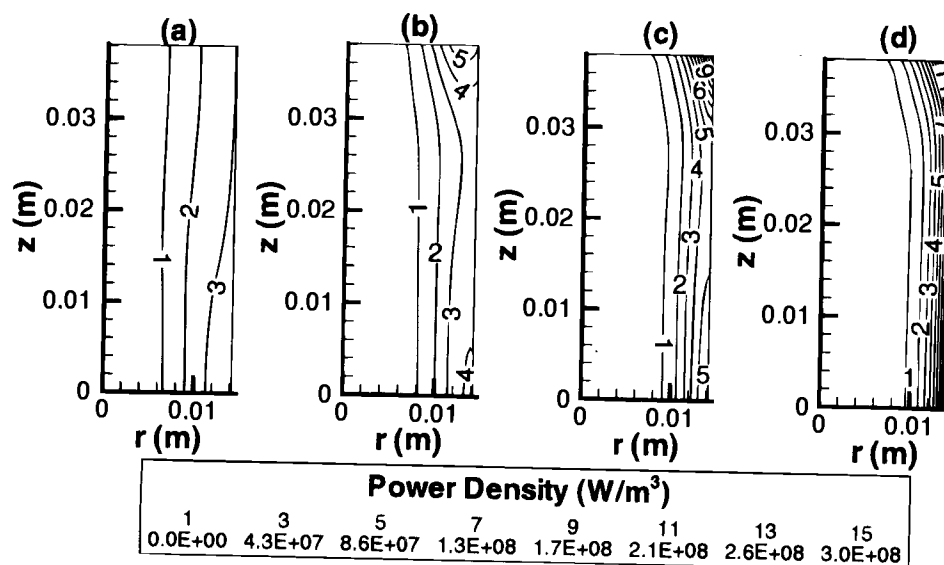
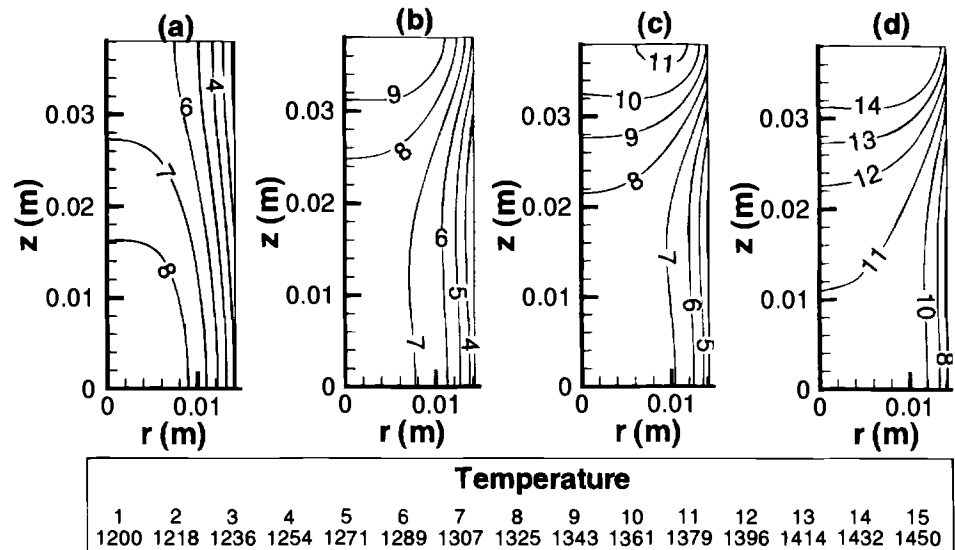


Fig. 14. Evolution of power density for RFCVI for modified conditions (insulation of axial ends, frequency 500 kHz, ramped power, absorbed power (W) = 4000 + 20*t* (h), operating pressure 760 Torr). Times are (a) 5, (b) 15, (c) 30, and (d) 81 h.

Fig. 15. Evolution of temperature for RFCVI with modified conditions (insulation of axial ends, frequency 500 kHz, ramped power, absorbed power (W) = 4000 + 20*t* (h), operating pressure 760 Torr). Times are (a) 5, (b) 15, (c) 30, and (d) 81 h.



with insulation at the ends of the preform compared to the RFCVI process without insulation. As more power is deposited at the ends of the preform, the temperature peak splits into two peaks which migrate along the axis to the

ends of the preform. At later times the center of the preform is cooler and eventually an off-axis peak in temperature is formed which signifies axial heat conduction to the central zone of the preform.

Fig. 16. Evolution of methane mole fraction for RFCVI with modified conditions (insulation of axial ends, frequency 500 kHz, ramped power, absorbed power (W) = 4000 + 20*t* (h), operating pressure 760 Torr). Times are (a) 5, (b) 15, (c) 30, and (d) 81 h.

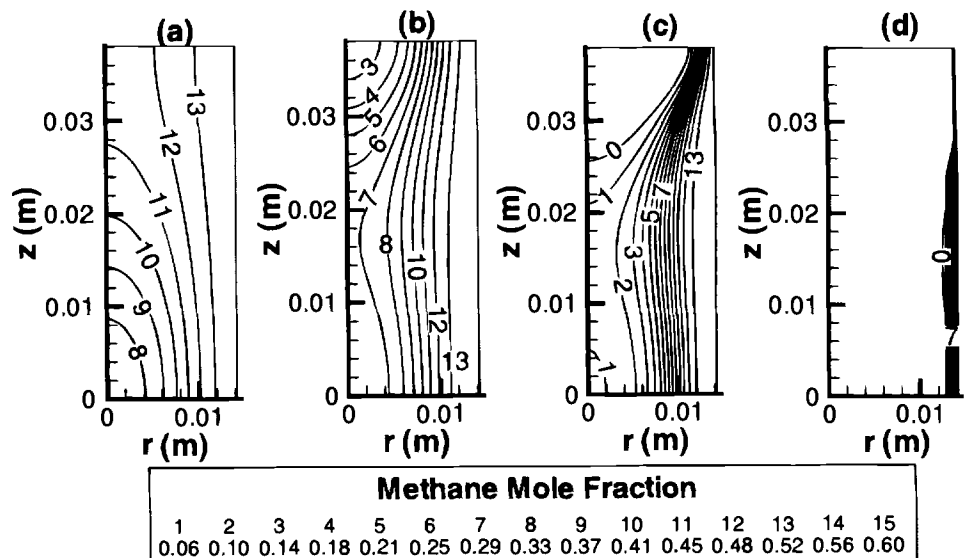
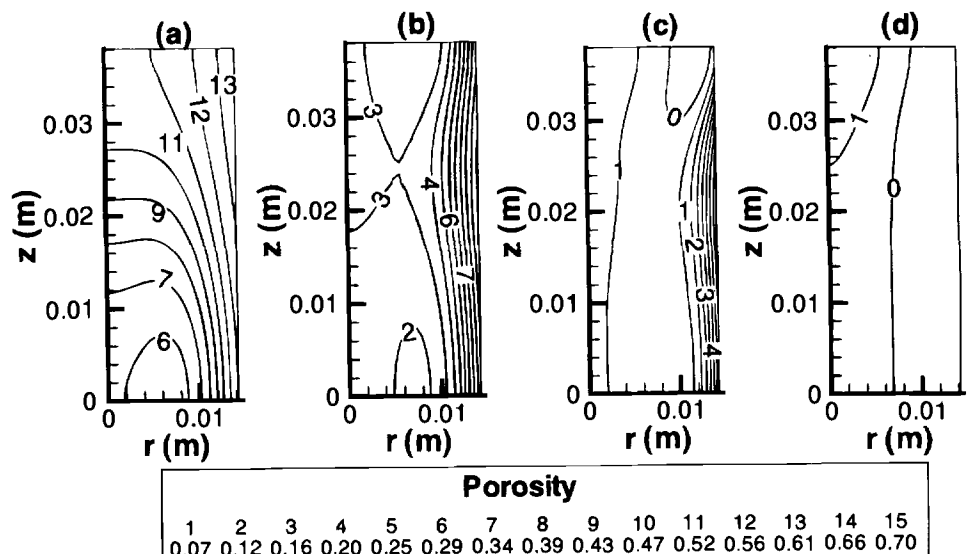


Fig. 17. Evolution of porosity for RFCVI with modified conditions (insulation of axial ends, frequency 500 kHz, ramped power, absorbed power (W) = 4000 + 20*t* (h), operating pressure 760 Torr). Times are (a) 5, (b) 15, (c) 30, and (d) 81 h.



The methane mole fraction (Fig. 16) evolves as the preform densifies and the temperature profile changes. Initially, the reactant is depleted as a peak in temperature is formed at the center of the preform. However, as the center temperature peak migrates to the ends of the preform, the center cools down and is replenished with reactant. This avoids the formation of entrapped porosity at the center of the preform. As the preform densifies further, a reactant concentration front is formed which moves radially outward. This is a direct consequence of the "inside-out" radial densification of the preform. Some entrapped porosity is formed at the ends of the preform due to localized heating, but the maximum porosity is about 0.07, which is much less than that observed with the original RFCVI process. Moreover, the location of this entrapped porosity is favorable, since the ends of the preform can become accessible to the reactant gas once the insulation is removed.

The performance of different strategies for improved RFCVI is shown in Fig. 18 which shows the change of spatially averaged (bulk) porosity under different operating conditions. Insulation at the ends of the preform with lower operating frequency leads to faster axial densification of the preform. However, only the rate of advancement of the axial densification front is improved. Thermal runaway still results in entrapment of porosity at the center of the preform. Increasing the frequency alone reduces thermal runaway but still results in predominantly axial densification of the preform as opposed to radial densification. Combining the effects of insulation and higher operating frequency is essential for achieving the radial densification pattern shown in Fig. 17. However, operation at a constant high power may lead to the entrapment of porosity located at the axial ends of the preform. By ramping the power, entrapped porosity at the ends of the preform is reduced significantly at the expense of lower rate of densification due to the relatively lower temperatures (curve marked insulation, ramped power, 500 kHz, 100 Torr in Fig. 18). Fortunately, as in the case of isothermal CVI for low operating temperature, porosity entrapment with the improved RFCVI scheme is relatively insensitive to the pressure. Therefore, a pressure of 760 Torr can be used with the modified RFCVI to enhance the rate densification without significant entrapment of porosity (curve marked insulation, ramped power, 500 kHz, 760 Torr in Fig. 18).

Figure 18 shows that a final bulk porosity of 0.06 can be achieved in about 60 h of modified RFCVI operation which represents a significant improvement over the 300 h required for isothermal operation. Furthermore, all the entrapped porosity is located at the ends of the preform for the modified RFCVI process, which becomes accessible once the insulation is removed. Clearly, RF heating has significant potential for reducing processing time com-

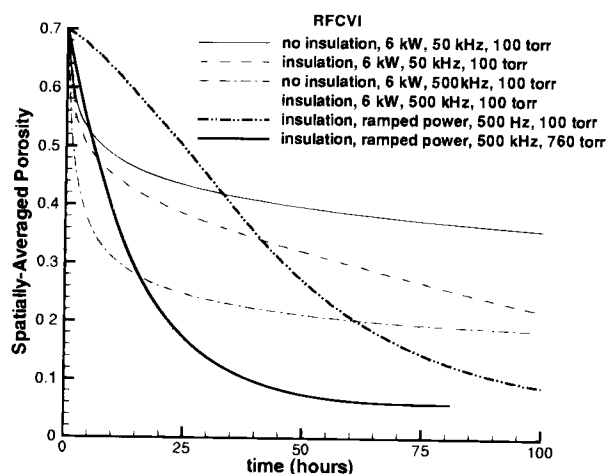


Fig. 18. Rate of densification (expressed as spatially averaged porosity vs. time) with RFCVI for different processing conditions.

pared to the conventional isothermal process. However, application of RF heating requires careful tailoring to meet the specific requirements of the preform geometry. A combination of several modifications, such as insulation of strategic sides of the preform, higher operating frequency, and ramping of power may be necessary to alter the densification behavior favorably. Models such as the 2D finite-element model used in this study provide useful tools for developing new schemes for improved performance. Clearly, experimental validation of the methodologies presented herein is necessary to fully access the potential of RFCVI and to evaluate the assumptions in the model. These experiments, in turn, should provide valuable insight into how the model can be improved. From the modeling point of view, future effort is directed toward examining the scale-up of RFCVI to larger preforms and applying this methodology to complex preform geometries and complex chemistries.

Conclusions

A 2D comprehensive finite-element model was used to study isothermal and RF-assisted CVI in a long cylindrical carbon preform.

1. Isothermal CVI was essentially 1D with densification directed from the edges of the preform to the center. The entrapped porosity was distributed along the entire volume of the core of the preform.

2. Direct RF heating of the preform may result in significant entrapment of porosity at the center. For a constant input power, densification occurs first radially around the central plane of the preform and then axially toward the two ends. This densification pattern produces only minimal densification at the center of the preform. Although fast rates of densification are possible initially, the overall time for completion may be significantly more for RFCVI processes than what is required for isothermal operation.

3. For RFCVI to be effective, tailoring of RF heating for the preform geometry is necessary. The combined effect of insulation at the ends of the preform, judicious choice of operating frequency, and ramping the power resulted in the radial "inside-out" densification of long cylindrical carbon preforms. Simulations show that processing time can be reduced fivefold with the modified scheme of RF heating compared to the conventional isothermal process.

Acknowledgments

This work was supported financially by a SRA/AFOSR contract and by the Energy Laboratory at the University of Houston.

Manuscript submitted November 11, 1997; revised manuscript received June 5, 1998.

The University of Houston assisted in meeting the publication costs of this article.

LIST OF SYMBOLS

B	permeability of preform, m^2
c	speed of light, m/s
C	gas concentration, $kmol/m^3$
C_s	solid concentration, $kmol/m^3$
C_i	gas concentration of i th species, $kmol/m^3$
Cp_i	heat capacity of the i th species, $J/(kg K)$
Cp_s	heat capacity of solid, $J/(kg K)$
D_i	Knudsen diffusivity of the i th species, m^2/s
D_i^e	effective Knudsen diffusivity of the i th species, m^2/s
D_{ij}	binary diffusivity of the i - j pair, m^2/s
D_{ij}^e	effective binary diffusivity of the i - j pair, m^2/s
E	electric field, V/m
E_1	reaction activation energy, $J/kmol$
E_n	azimuthal component of electric field, V/m
J_n	impressed current density, A/m^2
J_i	diffusive molar flux of the i th species, $kmol/(m^2 s)$
k_i	reaction rate constant, $1/s$
k^e	effective thermal conductivity, $W/(m-K)$
K_c	complex relative permittivity
M_s	solid molecular weight, $kg/kmol$
n	exponent for effective transport properties
n_H	heat flux, W/m^2
N_i	molar flux of the i th species, $kmol/(m^2 s)$

N_s	heat flux along preform surface, W/m^3
N_T	total molar flux, $kmol/(m^2 s)$
p	pressure, Pa
r	radial coordinate, m
r_f	fiber radius, m
r_p	pore radius, m
R	preform radius, m, also, gas constant, $(kg m^3)/(s^2 kmol K)$
s	Stefan-Boltzmann constant, $W/(m^2 K^4)$
t	time, s
t_p	processing time, s
T	temperature, K
W	power density, W/m^3
x_i	mole fraction of the i th species
z	axial coordinate, m
Z	coordination number

Greek

ϵ_0	dielectric constant of free space, F/m
ϵ	total porosity
ϵ^a	accessible preform porosity
ϵ_f	final spatially averaged porosity
ϵ_{max}	maximum value of porosity at the end of process
ϵ_p	porosity at percolation threshold
μ_0	magnetic permeability of free space, H/m
η	tortuosity factor for effective diffusivity
ρ_s	solid density, kg/m^3
σ^e	effective electrical conductivity, S/m
σ_s	electrical conductivity of solid, S/m
ω	angular frequency, rad/s

REFERENCES

- D. J. Devlin, R. P. Currier, R. S. Barbero, B. F. Espinoza, and N. Elliot, *Mater. Res. Soc. Symp. Proc.*, **250**, 233 (1992).
- K. Sugiyama and Y. Ohzawa, *J. Mater. Res.*, **25**, 4511 (1990).
- I. Golecki, in *Chemical Vapor Deposition XIII*, T. M. Besmann, M. D. Allendorf, McD. Robinson, and R. K. Ulrich, Editors, PV 96-5, p. 547, The Electrochemical Society Proceedings Series, Pennington, NJ (1996).
- D. J. Devlin, R. S. Barbero, and K. N. Siebein, in *Chemical Vapor Deposition XIII*, T. M. Besmann, M. D. Allendorf, McD. Robinson, and R. K. Ulrich, Editors, PV 96-5, p. 571, The Electrochemical Society Proceedings Series, Pennington, NJ (1996).
- D. Gupta and J. W. Evans, *J. Mater. Res.*, **6**, 810 (1991).
- J. I. Morell, D. J. Economou, and N. R. Amundson, *J. Electrochem. Soc.*, **139**, 328 (1992).
- J. I. Morell, D. J. Economou, and N. R. Amundson, *J. Mater. Res.*, **7**, 2447 (1992).
- J. I. Morell, D. J. Economou, and N. R. Amundson, *J. Mater. Res.*, **8**, 1067 (1993).
- J. Y. Ofori and S. V. Sotirchos, *J. Mater. Res.*, **11**, 2541 (1996).
- V. Midha and D. J. Economou, *J. Electrochem. Soc.*, **144**, 4062 (1997).
- R. Jackson, *Transport in Porous Catalysts*, Elsevier Publishing Company, New York (1977).
- C. A. Balanis, *Advanced Engineering Electromagnetics*, John Wiley & Sons, New York (1989).
- J. Y. Ofori and S. V. Sotirchos, *J. Electrochem. Soc.*, **144**, 275 (1997).
- S. M. Gutpte and J. A. Tsamopoulos, *J. Electrochem. Soc.*, **137**, 1626 (1990).
- J. Koplik, *J. Phys. C: Solid State Phys.*, **14**, 4821 (1981).
- M. Sahimi, *Applications of Percolation Theory*, Taylor and Francis, London (1994).
- F. Carmona, R. Conet, and P. Delhaes, *J. Appl. Phys.*, **61**, 2550 (1987).
- M. M. Tomadakis and S. V. Sotirchos, *AIChE J.*, **37**, 74 (1991).
- D. S. McLachlan, M. Blaszkiewicz, and R. E. Newnham, *J. Am. Ceram. Soc.*, **73**, 2187 (1990).
- S. V. Sotirchos, *AIChE J.*, **37**, 1365 (1991).
- J. Y. Ofori and S. V. Sotirchos, *J. Electrochem. Soc.*, **143**, 1962 (1996).
- T. J. R. Hughes, *The Finite Element Method*, Prentice-Hall, Englewood Cliffs, NJ (1987).
- A. C. Hindmarsh, *ACM-SIGNUM Newsletter*, **10** (1980).
- R. H. Perry and D. Green, *Perry's Chemical Engineers' Handbook*, 6th ed., McGraw-Hill Book Co., Singapore (1984).
- Engineered Materials Handbook, Composites*, Vol. 1, ASM International, OH (1987).
- J. Y. Ofori and S. V. Sotirchos, *AIChE J.*, **42**, 2828 (1996).